Journal of Inorganic and Organometallic Polymers and Materials (2019) 29:248–257
https://doi.org/10.1007/s10904-018-0983-8

Weakly Radio-Frequency Negative Permittivity of Poly(vinylidene fluoride)/Ti_3SiC_2 MAX Phase Metacomposites

Yao Liu[1] · Yunpeng Qu[1] · Jiahao Xin[2] · Zezhong Wang[3] · Guohua Fan[1] · Peitao Xie[1] · Kai Sun[2]

Received: 24 July 2018 / Accepted: 24 September 2018 / Published online: 25 September 2018
© Springer Science+Business Media, LLC, part of Springer Nature 2018

Abstract

While metal or carbon materials served as conductive phase in fabricating metamaterials or metacomposites have been widely investigated, MAX phases could provide alternative route. In this paper, Poly(vinylidene fluoride)/Ti_3SiC_2 MAX phase metacomposites with different Ti_3SiC_2 content were fabricated. Electrical and dielectric properties of metacomposites were analyzed. Percolating phenomenon was observed over the percolation threshold (f_c). Below f_c, ac conductivity spectra were explained by Jonscher's power law, indicating hopping conduction behavior. Above f_c, ac conductivity of composites follows Drude model, suggesting the metal-like conductive behavior. Weakly negative permittivity behavior was observed and explained by Lorentz and Drude model, suggesting the combinative contribution of induced electric dipole resonance and low-frequency plasmonic oscillation. The impedance performance of composites were also clarified by Nyquist plots and equivalent circuit analysis, manifesting the capacitive-inductive shift of composites. This work presented a novel route to metacomposites with weakly negative permittivity which greatly benefitted the practical applications of MAX phase in metacomposites.

Keywords Negative permittivity · Metacomposites · MAX phase · Metamaterials · PVDF

1 Introduction

The percolating theory was brought up initially in disordered systems to analyze sudden change of physical properties, broadening its application in heterogeneous materials. The percolation transition was generally presented in heterogeneous multicomponent composites. Actually, filler in composites was gradually contacted with each other leading to a continuous cluster throughout the composites when increasing filler content approaches f_c [1]. Accompanied with microstructure changing, percolative composites also underwent sudden change in some physical properties. For instance, positive/negative permittivity was tuned by controlling the functional phase content below/above f_c. Therefore, metacomposites with negative permittivity can be designed and fabricated following the percolative composite route.

Metamaterials with negative permittivity ϵ' have been extended into multiple novel applications which hardly can be realized by conventional materials [2]. Specifically, applications in perfect lens, invisible cloaking, wireless power transfer (WPT), magnetic resonance imaging and colossal permittivity materials [3] have been developed due to their exotically physical properties (e.g., negative refraction index, reversed Doppler effect and Vavilov–Cherenkov effect). In fact, the fascinating performance of metamaterials generally originates from their artificial and periodical metal structures (split-ring resonators, fishnets, wires or cut-wire pairs) [4–6]. Great achievements of metamaterials have been reported in recent years, some characteristics of metamaterials can be summarized.

Electronic supplementary material The online version of this article (https://doi.org/10.1007/s10904-018-0983-8) contains supplementary material, which is available to authorized users.

✉ Yao Liu
liuyao@sdu.edu.cn

✉ Kai Sun
kais@shmtu.edu.cn

[1] Key Laboratory for Liquid-Solid Structural Evolution and Processing of Materials (Ministry of Education), Shandong University, Jinan 250061, China

[2] College of Ocean Science and Engineering, Shanghai Maritime University, Shanghai 201306, China

[3] School of Mines, China University of Mining and Technology, Xuzhou 221000, China

For example, in order to tune the negative electromagnetic parameters, shape, size or geometric arrangement in metamaterials should be redesigned, leading to complex constructing process [3, 6–9]. Besides, anisotropic electromagnetic response in metamaterials will usually trigger an adverse impact when applied in electronics [10]. Metacomposites with random functional units were promising candidates to broaden the scope of metamaterials [11, 12], which can be fabricated by typical and traditional preparation technology of materials and could be designed on the basis of percolation theory.

When constructing metacomposites, metallic fillers (e.g., Fe, Ni, Cu or Ag) were usually served as conductive functional phases hosted in insulating matrixes. Negative parameters corresponding to the chemical composition and microstructure of metacomposites could be easily tuned [13, 14]. Negative permittivity could also be observed in metacomposites consisting of metallic alloys or amorphous alloys (e.g., $Fe_{50}Ni_{50}$, FeNiMo or $Fe_{78}Si_9B_{13}$) [15–17]. However, development of metal-based metacomposites were limited by the excessive power loss in composites and electromagnetic interference (EMI) to surrounding metal electronics [15, 18]. Under this circumstance, we presented a new route to metacomposites by consisting of nonmetallic conductive functional phases, "MAX" phases. $M_{n+1}AX_n$ phase was a group of layered ternary materials, where n is 1, 2 or 3, M is an early transition metal, A is an A-group element, and X is either C or N. MAX phases have triggered tremendous attentions due to their promising applications in structural reinforced ceramic matrix composites (CMCs), battery electrodes materials and supercapacitors [19–21]. MAX phases presented combination properties in metal and ceramic, including high-temperature oxidation resistance, damage tolerance, machinability, great electrical conductivity, and excellent irradiation/corrosion resistance [22–30]. Among all the MAX phases, Ti_3SiC_2 exhibits great electrical conductivity and structural performance which makes it a promising candidate for preparing metacomposites [19]. Poly(vinylidene fluoride) (PVDF) was a semicrystalline thermoplastic polymer with high piezo- and pyroelectric coeefficients, great thermal and chemical resistance. PVDF has been employed into percolative composites with colossal permittivity by containing functional phases (e.g., $BaTiO_3$, PZT) [31–51]. Therefore, PVDF and Ti_3SiC_2 MAX phase was selected as matrix and functional phase respectively to fabricate percolative metacomposites towards negative permittivity.

In this work, Ti_3SiC_2/PVDF metacomposites with different Ti_3SiC_2 content were prepared. The electrical and dielectric properties were investigated at radio frequency range (20 MHz–1 GHz). The different variation trends of ac conductivity spectra verified the percolation threshold. Negative permittivity behavior was observed in composites above f_c. Equivalent circuit models were applied to analyze the impedance response of Ti_3SiC_2/PVDF composites.

2 Materials and Methods

Ti_3SiC_2 (purity > 98%, average size ~ 44 μm) were purchased from Haoxinano Technology Co., Ltd. Poly(vinylidene fluoride) were acquired from Shenzhen Boyi Plastic Raw Material Co., Ltd. The composites with Ti_3SiC_2 content of 10 wt%, 30 wt%, 50 wt%, 60 wt%, 70 wt%, 80 wt%, and 85 wt% were prepared by blending and compression molding procedure. Field emission scanning electron microscopy (FESEM) and X-ray diffractometer (XRD) with Cu K_α radiation were applied to characterize microstructure and phase composition of composites. The electrical and dielectric properties of composites was tested by Agilent E4991A precision impedance analyzer. The detailed testing and calculating process was presented in Supplementary Information.

3 Results and Discussion

3.1 Microstructure and Composition Characterization

Figure 1 shows SEM images of Ti_3SiC_2/PVDF metacomposites at different Ti_3SiC_2 filling content. The isolated Ti_3SiC_2 particles are randomly distributed in PVDF matrix. As increasing Ti_3SiC_2 content, the Ti_3SiC_2 particles gradually interconnect with each other leading to the formation of three-dimensional (3D) conductive networks in Ti_3SiC_2/PVDF composites (85 wt%). Figure 2 shows XRD patterns of Ti_3SiC_2 and Ti_3SiC_2/PVDF composites with different Ti_3SiC_2 content. The XRD pattern of PVDF materials was indexed by α, β, and γ crystal phases of PVDF. The peak at 18.4° was corresponding to the α-phase. The peaks of 20.8° and 26.6° indicated the β-phase superposition and γ-phase diffraction respectively. As increasing Ti_3SiC_2 content, the diffraction peaks of PVDF were wakening while the diffraction peaks of Ti_3SiC_2 were enhancing. FT-IR experiments of raw PVDF materials were performed as shown in Fig. 3a. The FT-IR spectra showed the typical absorption peaks of α-phase, β-phase, and γ-phase of PVDF at about 613 cm^{-1}, 488 cm^{-1} and 841 cm^{-1}, respectively. The bending of C–C–C is observed at 1071 cm^{-1}, and the peak of CH_2 appears at 1403 cm^{-1}. Figure 3b shows the simultaneous DSC/TGA curves of PVDF raw materials measured at heating rate 10 K/min in air. As temperature rising, the weight of PVDF materials kept unchanged below 350 °C and then starting losing weight. DSC curve shows an endothermic peak at about 380 °C and an exothermic peak at about 485 °C which could be attributed to the decomposition of

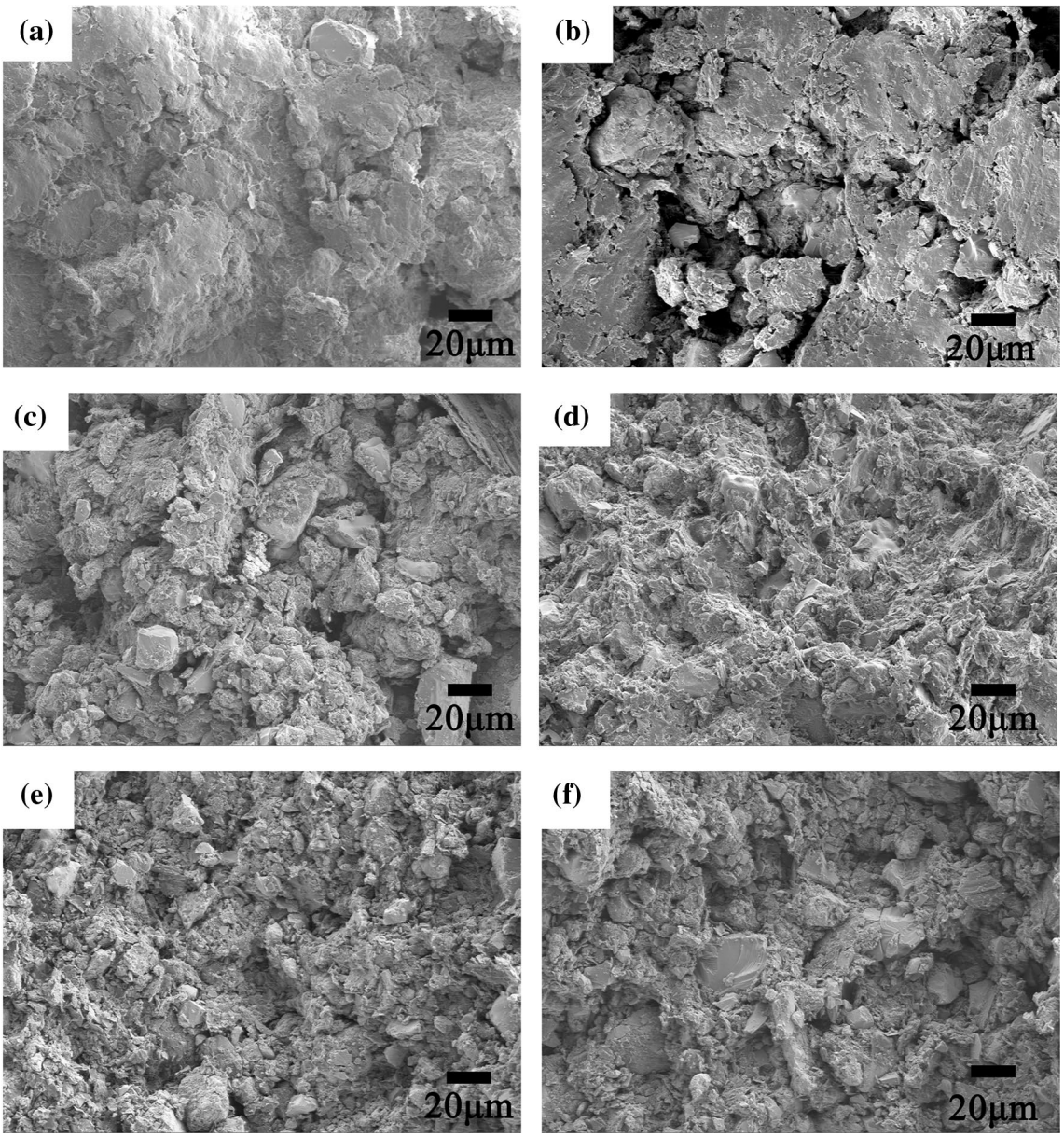

Fig. 1 SEM images of Ti_3SiC_2/PVDF metacomposites with Ti_3SiC_2 content of 10 wt% (**a**), 30 wt% (**b**), 50 wt% (**c**), 70 wt% (**d**), 80 wt% (**e**), and 85 wt% (**f**)

PVDF. PVDF becomes exothermic over 450 centigrade, suggesting that the heat quantity originating from PVDF decomposed reaction was larger than that from PVDF melting.

3.2 Conductivity Behavior

Figure 4 shows the frequency dependences of ac conductivity (σ_{ac}) in Ti_3SiC_2/PVDF metacomposites with different Ti_3SiC_2 content. σ_{ac} increased on frequency rising when Ti_3SiC_2 contents were lower than that of 80 wt% in composites, while σ_{ac} decreased with frequency for composites at higher filling content. It is noteworthy that σ_{ac} sharply increases (ϵ' sharply decreases) when Ti_3SiC_2 content range from 80 to 85 wt% as shown in Fig. 5d. Further to say, the different variation trends of σ_{ac} versus frequency indicated different conductive mechanisms. Percolation behavior occurred in Ti_3SiC_2/PVDF composites on raising Ti_3SiC_2 content. The percolation threshold f_c was between 80 and 85 wt%, which was verified by the different conductive model. For composites below f_c, the $\sigma_{ac} - f$ relationship can be expressed as:

$$\sigma_{ac} = \sigma_{dc} + A(2\pi f)^n \quad (1)$$

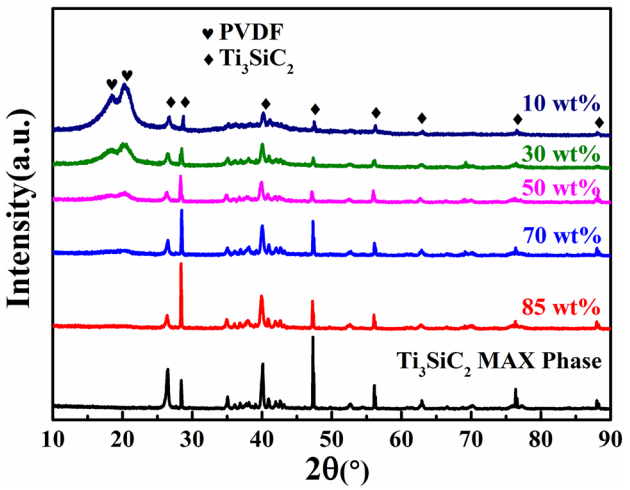

Fig. 2 XRD patterns of Ti_3SiC_2 and Ti_3SiC_2/PVDF composites with different Ti_3SiC_2 content

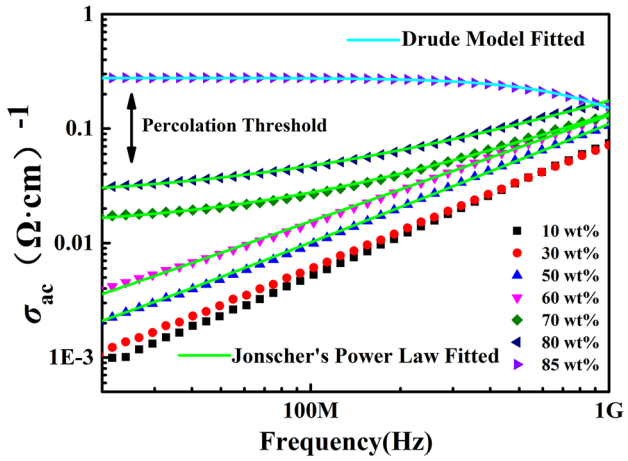

Fig. 4 Frequency dispersions of ac conductivity for the Ti_3SiC_2/PVDF composites

where σ_{dc} is direct current conductivity, f is the frequency, A is the pre-exponential factor and n is the fractional exponent ($0 < n < 1$). For composites (10 wt%, 30 wt%, 50 wt% and 60 wt%), ac conductance was primary over whole test frequency as shown in Fig. 4. As increasing Ti_3SiC_2 content to 70 wt% and 80 wt%, dc conductance dominated at low frequency region and ac conductance was primary at high frequency range. The fitting parameters were also confirmed the above analysis shown in Table S3. Experiencing an external electric field (especially high-frequency electric field), free electrons can "jump" across adjacent Ti_3SiC_2 particles which was denoted as hopping conduction behavior. When the Ti_3SiC_2 content exceeded f_c, the Ti_3SiC_2 particles were interconnected to each other leading to the formation of 3D conductive networks throughout the composites. MAX phase presented metallic conduction (denoted as metal-like conduction behavior), i.e., σ_{ac} was almost independent of frequency at low frequencies while σ_{ac} decreased at high frequencies. Skin effect was applied to explain the metallic conduction. The skin depth was expressed as:

$$\delta = \left(\frac{2}{\omega\mu\sigma_{dc}}\right)^{\frac{1}{2}} \tag{2}$$

where δ is the skin depth, ω is the angular frequency, σ_{dc} is the dc conductivity, and $\mu$is the static permeability of the composites. The increasing frequency reduced the skin depth resulting in enhancement of the skin effects. The metal-like conductive behavior of composites with Ti_3SiC_2 content of 85 wt% was explained by Drude model:

$$\sigma_{ac} = \frac{\sigma_{dc}\omega_{\tau}^2}{\omega^2 + \omega_{\tau}^2} \tag{3}$$

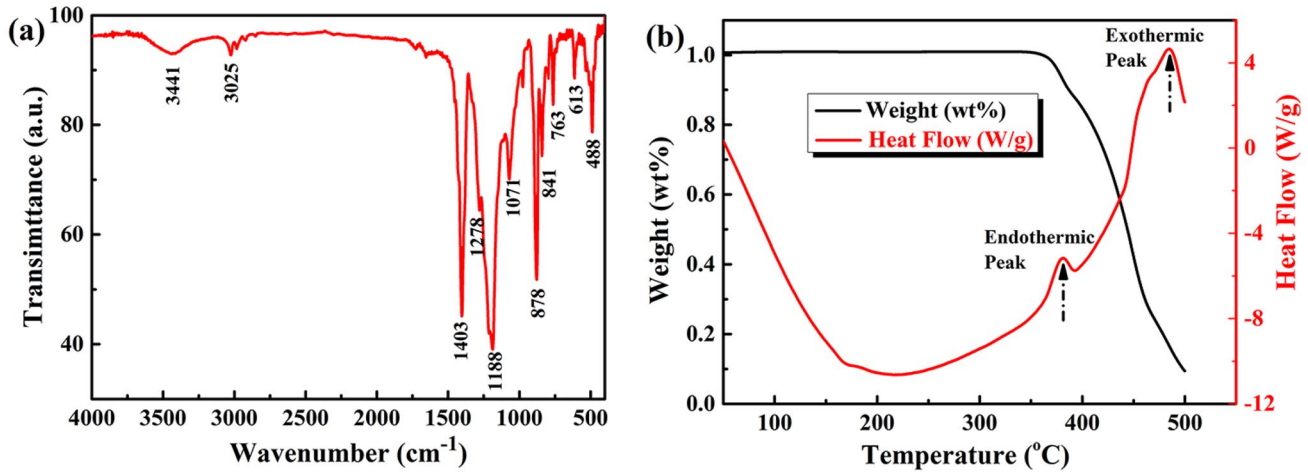

Fig. 3 FT-IR curves of PVDF raw materials (**a**) and simultaneous DSC/TGA curves for PVDF raw materials (**b**)

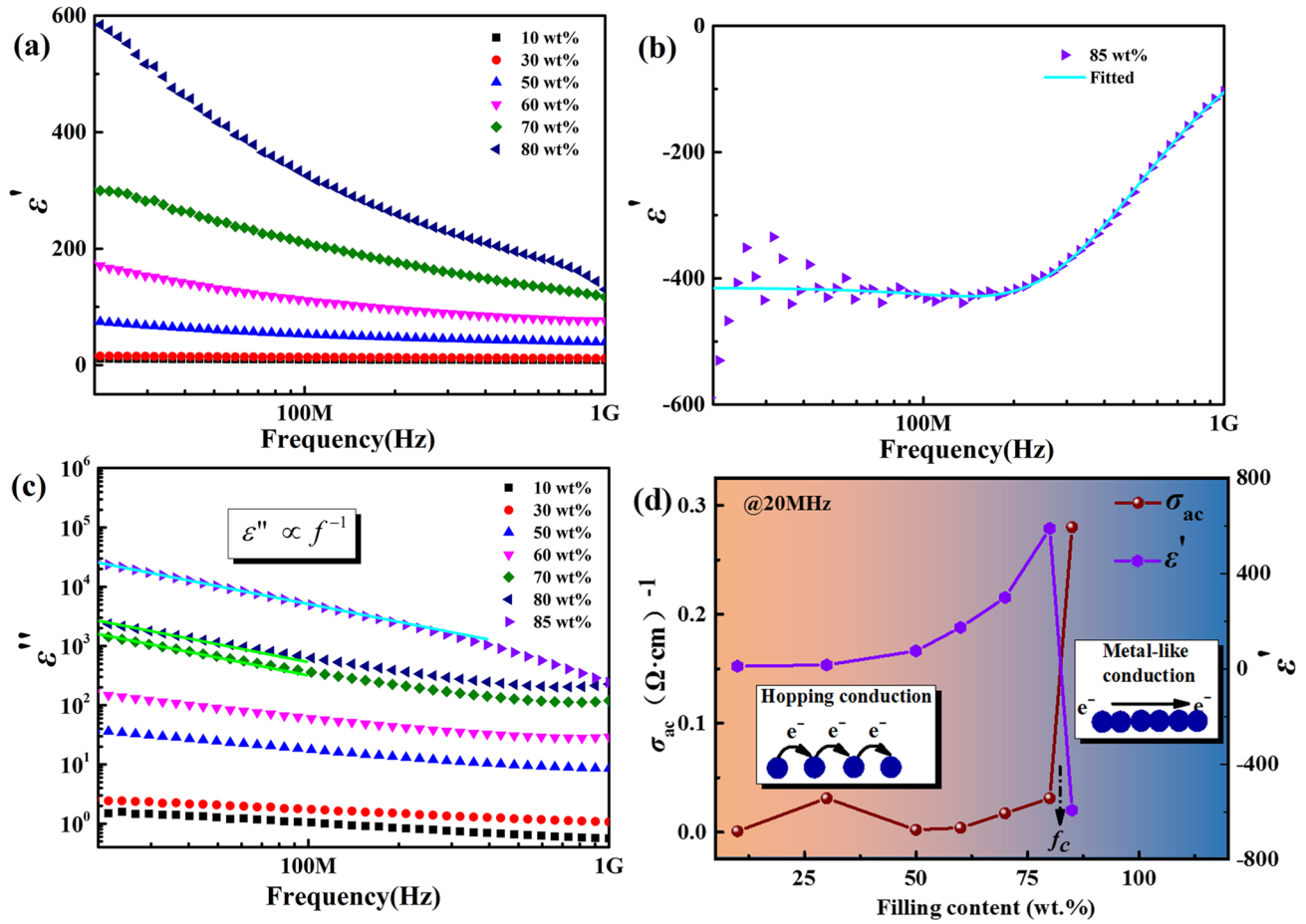

Fig. 5 Frequency dependences of real permittivity ($\epsilon^{'}$) for Ti_3SiC_2/PVDF composites (**a, b**). Frequency dispersions of the imaginary permittivity (ϵ'') (**c**). Variation trends of ac conductivity and real permittivity at 20 MHz with different Ti_3SiC_2 filling content (**d**)

$$\sigma_{dc} = \frac{Ne^2\tau}{m} = \frac{\omega_p^2\tau}{4\pi} \tag{4}$$

where σ_{dc} is the dc limitation in conductivity, $\omega_\tau\,(\omega_\tau = 1/\tau)$ is the relaxation rate, and ω_p describes the oscillator strength.

3.3 Negative Permittivity Behavior

Frequency dependences of the real permittivity ($\epsilon^{'}$) of Ti_3SiC_2/PVDF with different Ti_3SiC_2 content were showed in Fig. 5a, b. For composites below the percolation threshold f_c, the values of $\epsilon^{'}$ were positive and enhanced with increasing Ti_3SiC_2 content at 20 MHz–1 GHz region shown in Fig. 5a, d, which could be ascribed to increasing interface connection of isolated Ti_3SiC_2 particles and PVDF matrix in the composites. Further, interfacial polarization in these micro-capacitors formed by Ti_3SiC_2 particles and PVDF matrix, denoted as Maxwell–Wagner–Sillars effect, was responsible for the improvement of permittivity.

As analyzed above, negative permittivity behavior observed over f_c in composites, was ascribed to the formation of 3D interconnected Ti_3SiC_2 networks. Ti_3SiC_2 networks in composites with metallic conduction, generally presented low frequency plasmonic state leading to plasma-type negative permittivity behavior. The plasma-type negative permittivity behavior was theoretically described by Drude model as follows:

$$\varepsilon^* = \varepsilon' - i\varepsilon'' = 1 - \frac{\omega_p^2}{\omega^2 + i\omega\Gamma_D} \tag{5}$$

$$\varepsilon' = 1 - \frac{\omega_p^2}{\omega^2 + \Gamma_D^2} \tag{6}$$

$$\omega_p = \sqrt{\frac{n_{eff}e^2}{m_{eff}\varepsilon_0}} \tag{7}$$

where, Γ_D is the damping constant, $\omega_p = 2\pi f_p$ is plasmons angular frequency, n_{eff} is effective concentration of electron, and m_{eff} is effective weight of electron. However, as shown in Fig. S1, Drude model was not in agreement with the negative permittivity spectra at low frequency regions, suggesting that there should be another generation mechanism. Considering the combinative metallic and ceramic properties of MAX phase, there may be impactions of induced electric dipole at low frequency range. Thus, we combined Lorentz model with Drude model to explain negative permittivity behavior. The Lorentz model was expressed as:

$$\varepsilon^* = \varepsilon' - i\varepsilon'' = 1 + \frac{\omega_p^2}{\omega_0^2 + \omega^2 + i\Gamma_L\omega} \tag{8}$$

$$\varepsilon' = 1 + \frac{\omega_p^2\left(\omega_0^2 - \omega^2\right)}{\left(\omega_0^2 - \omega^2\right)^2 + \omega^2\Gamma_L^2} \tag{9}$$

where $\omega\,(\omega = 2\pi f)$ is the angular frequency, $\omega_0\,(\omega_0 = 2\pi f_0)$ is the characteristic frequency, $\omega_p\,(\omega_p = 2\pi f_p)$ is the angular plasma frequency, and Γ_L represents the damping constant. The Lorentz type dielectric resonance was resulted from the induced electric dipole in the isolated Ti_3SiC_2 particles. As shown in Fig. 5b, negative permittivity spectra was fitted well by combination of Drude model and Lorentz model.

Dielectric loss in composites evaluated by imaginary permittivity (ϵ'') was an important performance when applied in electronic devices. In percolative composites, electric field frequency and concentration of conductive fillers were primary influencing factor to dielectric loss. Generally, dielectric loss mainly includes the conduction loss ε_C'', polarization loss ε_P'' and dipole loss ε_D'', which was expressed as:

$$\varepsilon'' = \varepsilon_C'' + \varepsilon_D'' + \varepsilon_P'' \tag{10}$$

At 20 MHz–1 GHz region, the conduction loss and dipolar loss were primary loss. ε_C'' originating from leakage current among conductive fillers was expressed as:

$$\varepsilon_C'' = \frac{\sigma_{dc}}{2\pi f\varepsilon_0} \tag{11}$$

where σ_{dc} is a constant. Thus, ε_C'' was inversely related to f ($\varepsilon_C'' \propto f^{-1}$). Figure 5c presented frequency dependent $\epsilon''$for the Ti_3SiC_2/PVDF composites with different filling content. $\epsilon''$was evidently enhanced ascribing to the incorporation of conductive Ti_3SiC_2 particles. For the composites below f_c, ϵ'' spectra exhibited liner decrease trend in low frequency. With increasing frequency, relationship of ϵ'' versus f presented nonlinear increasing trend. In other words, the dominant role in dielectric loss changed from the ε_C'' to the ε_D'' with frequency rising.

3.4 Impedance and Equivalent Circuit Analysis

For Ti_3SiC_2/PVDF composites with positive permittivity, the reactance showed negative values at 20 MHz–1 GHz region (Fig. 6a). The relationship for different circuit elements was expressed as:

$$Z = \frac{\dot{U}}{\dot{I}} = R + i\left(X_L - X_C\right) = Z' + iZ'' \tag{12}$$

$$\varphi = \arctan\frac{\dot{U}_X}{\dot{U}_R} = \arctan\frac{\dot{U}_L - \dot{U}_C}{\dot{U}_R} \tag{13}$$

That is to say, for composites below f_c, capacitive reactance was stronger than inductive reactance ($Z'' = X_L - X_C < 0$) indicating capacitive character. Equivalent

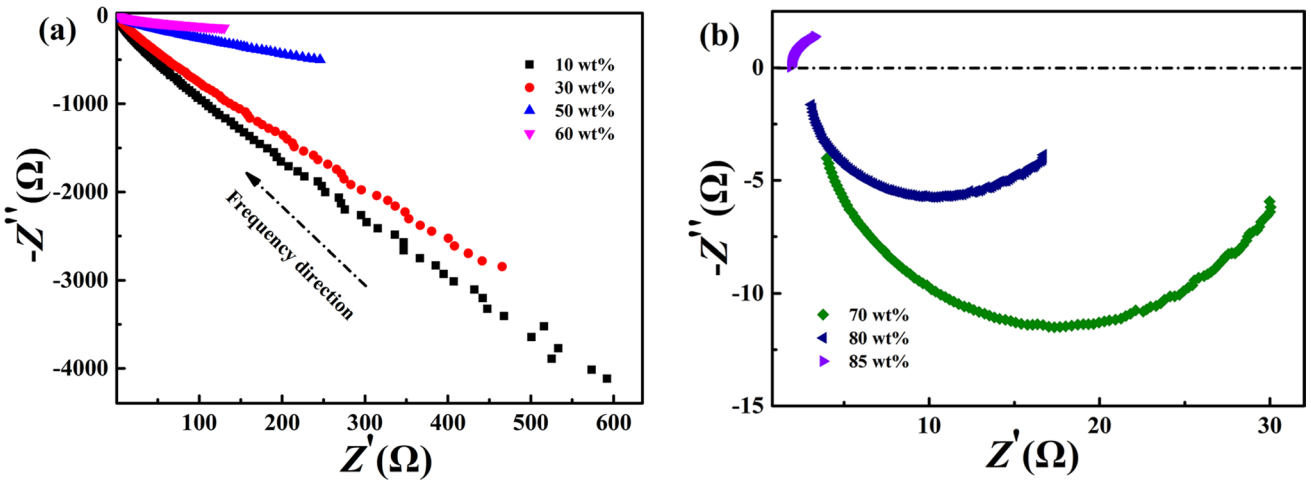

Fig. 6 Nyquist plots (**a, b**) for the Ti_3SiC_2/PVDF composites with different Ti_3SiC_2 content

circuit models was applied to analyze impedance response of Ti_3SiC_2/PVDF composites. Equivalent circuit model of composites below f_c consists of a series resistor (R_s) and a parallel connection of a resistor (R_p) and a capacitor (C_p) (inset of Fig. 7a). R_p, originating from the leakage current of composites, decreased with increasing conductive Ti_3SiC_2 particles in PVDF matrix. C_p, mainly deriving from the micro-capacitors constructed by the Ti_3SiC_2 and PVDF particles in composites, increased on increasing Ti_3SiC_2 content. Noteworthy, C_p sharply increased near f_c. While capacitive reactance for composites above f_c was less than inductive reactance ($Z'' = X_L - X_C > 0$) leading to inductive character. Equivalent circuit model of composites above f_c consists of resistors (R_p, R_1 and R_2), capacitor (C_p), and inductors (L_1 and L_2) as shown in Fig. 7a. As illustrated in Fig. 8a, b, isolated Ti_3SiC_2 particles distributed in PVDF matrix were equivalently forming to capacitors, while conductive paths of inductors in composites were formed by connective Ti_3SiC_2 particles.

Figure 7b presented frequency dependent φ for Ti_3SiC_2/PVDF composites with different filling content. When composites experiencing ac electric field, the samples was

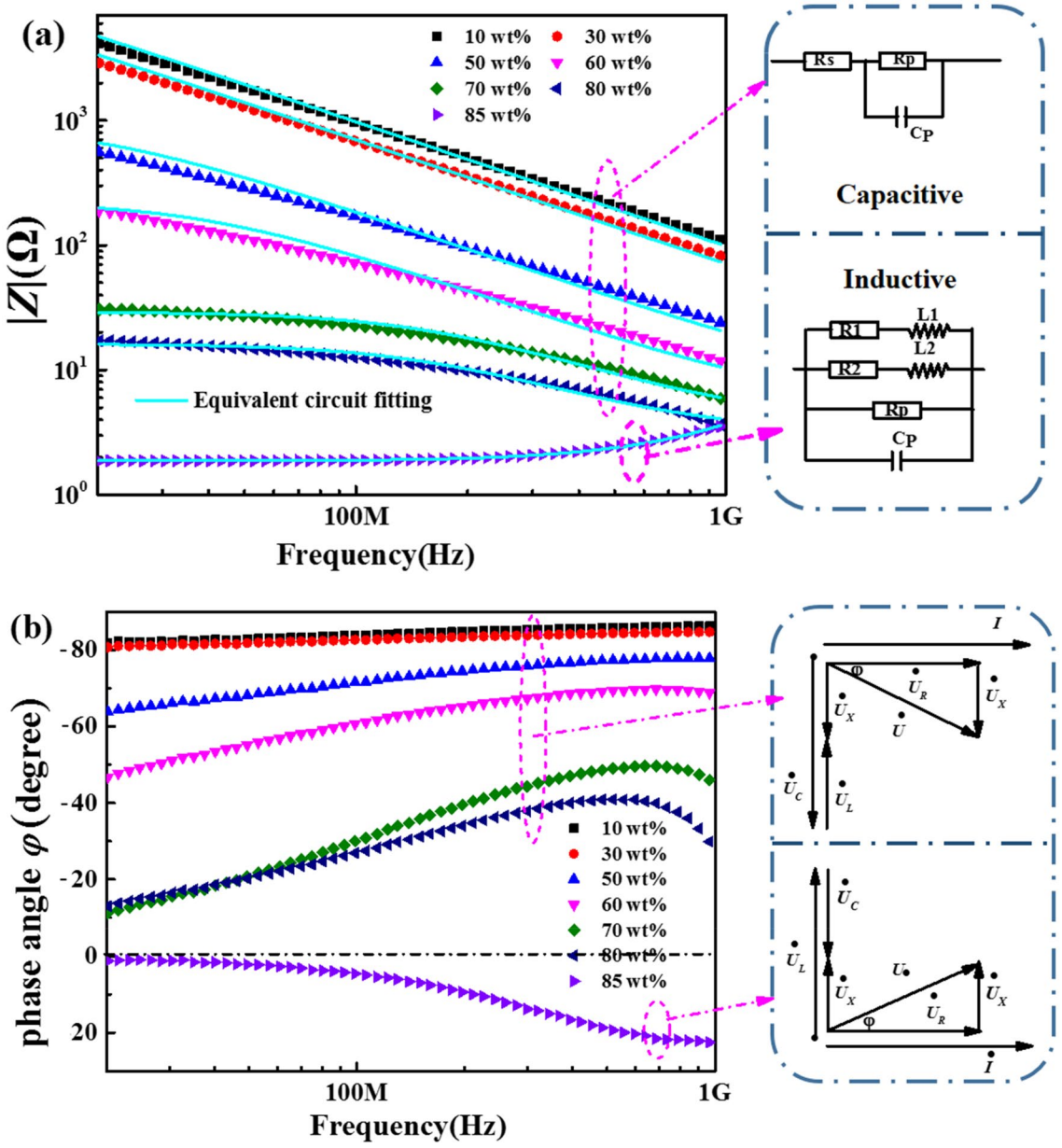

Fig. 7 Frequency dependent impedance (**a**) and phase angle φ (**b**) for Ti_3SiC_2/PVDF composites. Phasor diagrams of voltage versus current were presented in **b**. U, I, U_R, U_L, U_X and U_C are voltage or current phasor for different circuit elements, φ is the impedance angle, X_L, X_C and X are reactance

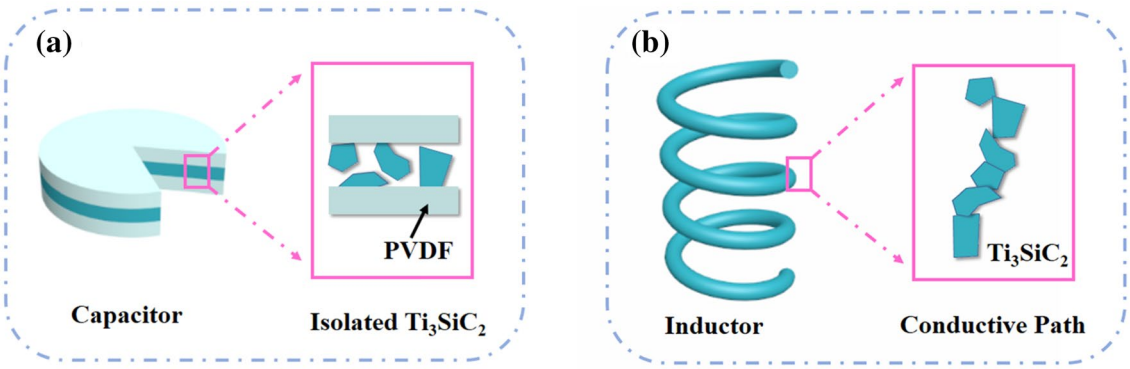

Fig. 8 Schematic evolution of the microstructure corresponding with variation of capacitor (**a**) and inductor (**b**)

considered as a typical *RLC* circuit consisting of capacitors (*C*), resistors (*R*) and/or inductors (*L*) shown in Fig. S3 in Supplementary Materials. When sample is pure resistor, the voltage and current is synchronous and $\varphi = 0°$. Generally, when sample presents capacitive or inductive, the current and voltage is unsynchronized. Specifically, when the current and voltage flows through a capacitor, voltage lags current by 90° ($\varphi = -90°$). While, the current lags voltage by 90° ($\varphi = 90°$) as the current and voltage flows through an inductor. In Ti_3SiC_2/PVDF composites, φ shifts from negative to positive on increasing Ti_3SiC_2 content, indicating transition of capacitive to inductive. For composite below f_c, the φ values are range from −90° to 0°. Under this circumstance, $\underset{L}{\dot{U}} < \underset{C}{\dot{U}}$, thus $U_X < 0$, suggests that voltage phase falls behind the current phase, capacitors dominate in the circuit and composite manifests capacitive character. Correspondingly, composites above f_c present inductive character when phase shift angle φ values range from 0° to 90°. Under this circumstance, $\underset{L}{\dot{U}} > \underset{C}{\dot{U}}$, thus $U_X > 0$, indicates that current phase lags behind voltage phase, inductors dominates in the circuit and composite manifests inductive character.

4 Conclusion

In conclusion, Ti_3SiC_2/PVDF percolative metacomposites towards negative permittivity were prepared. Conductive mechanism changes when increasing Ti_3SiC_2 content over f_c. Negative permittivity behavior was explained by Lorentz and Drude model, suggesting the combinative contribution of induced electric dipole resonance and low-frequency plasmonic oscillation at radio-frequency region. Equivalent circuit analysis to impedance response of metacomposites manifested correspondence between capacitive-inductive characteristic change and positive–negative permittivity change. This work facilitates clarifying the generation mechanism of negative permittivity which will greatly extend applications of MAX phase in metacomposites.

Acknowledgements This study was financially supported by the National Natural Science Foundation of China [Grant Nos. 51771104 and 51402170].The author Yunpeng Qu thanks Murakami Haruki, Franz Kafka and Higashino Keigo whose novels comforted the author's soul. The author Yunpeng Qu also thanks Prof. Shaohua Lin from Ocean University of China (OUC) whose replying letter encouraged Qu to work for the graduate degree.

References

1. D.J. Bergman, D. Stroud, Physical properties of macroscopically inhomogeneous media. Solid State Phys. **46**, 147–269 (1992)
2. D.R. Smith, J.B. Pendry, M.C. Wiltshire, Metamaterials and negative refractive index. Science **305**, 788–792 (2004)
3. B. Wang, K.H. Teo, T. Nishino, W. Yerazunis, J. Barnwell, J. Zhang, Experiments on wireless power transfer with metamaterials. Appl. Phys. Lett. **98**, 254101–254103 (2011)
4. S. Jahani, Z. Jacob, All-dielectric metamaterials. Nat. Nanotechnol. **11**, 23–36 (2016)
5. N.K. Grady, J.E. Heyes, D.R. Chowdhury, Y. Zeng, M.T. Reiten, A.K. Azad, A.J. Taylor, D.A. Dalvit, H.T. Chen, Terahertz metamaterials for linear polarization conversion and anomalous refraction. Science **340**, 1304–1307 (2013)
6. W.J. Padilla, D.N. Basov, D.R. Smith, Negative refractive index metamaterials. Mater. Today **9**, 28–35 (2006)
7. S. Linden, C. Enkrich, M. Wegener, J. Zhou, T. Koschny, C.M. Soukoulis, Magnetic response of metamaterials at 100 terahertz. Science **306**, 1351–1353 (2004)
8. V.M. Shalaev, T.A. Klar, V.P. Drachev, A.V. Kildishev, Optical negative-index metamaterials: from low to no loss. Nat. Photon. **1**, 41–48 (2006)
9. D.R. Smith, J.B. Pendry, M.C.K. Wiltshire, Metamaterials and negative refractive index. Science **305**, 788–792 (2004)
10. X. Zhang, Metamaterials for perpetual cooling at large scales. Science **355**, 1023–1024 (2017)
11. M. Chen, X. Wang, Z. Zhang, K. Sun, C. Cheng, F. Dang, Negative permittivity behavior and magnetic properties of C/YIG composites at radio frequency. Mater. Des. **97**, 454–458 (2016)
12. N.D. Gavrilova, V.K. Novik, A.V. Vorobyev, I.A. Malyshkina, Negative dielectric permittivity of poly(acrylic acid) pressed pellets. J. Non-Cryst. Solids **452**, 1–8 (2016)

13. Z. Zhang, R. Fan, Z. Shi, S. Pan, K. Yan, K. Sun, J. Zhang, X. Liu, X.L. Wang, S.X. Dou, Tunable negative permittivity behavior and conductor–insulator transition in dual composites prepared by selective reduction reaction. J. Mater. Chem. C **1**, 79–85 (2013)
14. Z. Zhang, K. Sun, Y. Liu, Z. Kuang, S. Sun, X. Ji, The negative permittivity behavior and magnetic property of $FeNi/Al_2O_3$ composites in radio frequency region. Ceram. Int. **42**, 19063–19065 (2016)
15. M. Chen, R.H. Fan, M. Gao, S.B. Pan, M.X. Yu, Z.D. Zhang, Negative permittivity behavior in $Fe_{50}Ni_{50}/Al_2O_3$ magnetic composite near percolation threshold. J. Magn. Magn. Mater. **381**, 105–108 (2015)
16. M. Chen, M. Gao, F. Dang, N. Wang, B. Zhang, S. Pan, Tunable negative permittivity and permeability in $FeNiMo/Al_2O_3$ composites prepared by hot-pressing sintering. Ceram. Int. **42**, 6444–6449 (2016)
17. Q. Hou, K.L. Yan, R.H. Fan, Z.D. Zhang, M. Chen, K. Sun, C.B. Cheng, Experimental realization of tunable negative permittivity in percolative $Fe_{78}Si_9B_{13}$/epoxy composites. RSC Adv. **5**, 9472–9475 (2015)
18. X.A. Wang, Z.C. Shi, M. Chen, R.H. Fan, K.L. Yan, K. Sun, S.B. Pan, M.X. Yu, Tunable electromagnetic properties in Co/Al_2O_3 cermets prepared by wet chemical method. J. Am. Ceram. Soc. **97**, 3223–3229 (2014)
19. M.A. Piechowiak, J. Henon, O. Durand-Panteix, G. Etchegoyen, V. Coudert, P. Marchet, F. Rossignol, Growth of dense Ti_3SiC_2 MAX phase films elaborated at room temperature by aerosol deposition method. J. Eur. Ceram. Soc. **34**, 1063–1072 (2014)
20. L.L. Zheng, L.C. Sun, M.S. Li, Y.C. Zhou, Improving the high-temperature oxidation resistance of $Ti_3(SiAl)C_2$ by Nb-doping. J. Am. Ceram. Soc. **94**, 3579–3586 (2011)
21. J.L. Smialek, Environmental resistance of a Ti_2AlC-type MAX phase in a high pressure burner rig. J. Eur. Ceram. Soc. **37**, 23–34 (2017)
22. R. Yin, H. Wu, K. Sun et al., Fabrication of graphene network in alumina ceramics with adjustable negative permittivity by spark plasma sintering. J. Phys. Chem. C **122**, 1791–1799 (2018)
23. R. Yin, Y. Zhang, W. Zhao et al., Graphene platelets/aluminium nitride metacomposites with double percolation property of thermal and electrical conductivity. J. Eur. Ceram. Soc. **38**, 4701–4706 (2018)
24. H. Wu, R. Yin, Y. Zhang et al., Synergistic effects of carbon nanotubes on negative dielectric properties of graphene-phenolic resin composites. J. Phys. Chem. C **121**, 12037–12045 (2017)
25. H. Wu, R. Yin, L. Qian et al., Three-dimensional graphene network/phenolic resin composites towards tunable and weakly negative permittivity. Mater. Des. **117**, 18–23 (2017)
26. H. Wu, Y. Zhang, R. Yin et al., Magnetic negative permittivity with dielectric resonance in random Fe_3O_4@graphene-phenolic resin composites. Adv. Compos. Hybrid Mater. **1**, 168–176 (2018)
27. H. Wu, Y. Qi, Z. Wang et al., Low percolation threshold in flexible graphene/acrylic polyurethane composites with tunable negative permittivity. Compos. Sci. Technol. **151**, 79–84 (2017)
28. P. Xie, Z. Wang, Z. Zhang et al., Silica microspheres templated self-assembly of three-dimensional carbon network with stable radio-frequency negative permittivity and low dielectric loss. J. Mater. Chem. C **6**, 5239–5249 (2018)
29. P. Xie, K. Sun, Z. Wang et al., Negative permittivity adjusted by SiO_2-coated metallic particles in percolative composites. J. Alloy. Compd. **725**, 1259–1263 (2017)
30. Z. Guo, P. Xie, F. Dang et al., Bio-gel derived nickel/carbon nanocomposites with enhanced microwave absorption. J. Mater. Chem. C **6**, 8812–8822 (2018)
31. P. Xie, W. Sun, Y. Liu et al., Carbon aerogels towards new candidates for double negative metamaterials of low density. Carbon **129**, 598–606 (2018)
32. Z. Zhao, R. Guan, J. Zhang, Z. Zhao, P. Bai, Effects of process parameters of semisolid stirring on microstructure of Mg-3Sn-1Mn-3SiC (wt%) strip processed by rheo-rolling. Acta Metall. Sin. **30**, 66–72 (2017)
33. Z. Zhao, P. Bai, R. Guan, V. Murugadoss, H. Liu, X. Wang, Z. Guo, Microstructural evolution and mechanical strengthening mechanism of Mg-3Sn-1Mn-1La alloy after heat treatments. Mater. Sci. Eng. A **734**, 200–209 (2018)
34. T. Su, Q. Shao, Z. Qin, Z. Guo, Z. Wu, Role of interfaces in two-dimensional photocatalyst for water splitting. ACS Catal. **8**, 2253–2276 (2018)
35. Z. Sun et al., Experimental and simulation understanding of morphology controlled barium titanate nanoparticles under co-adsorption of surfactants. CrystEngComm **19**, 3288–3298 (2017)
36. L. Zhang, W. Yu, C. Han, J. Guo, Q. Zhang, H. Xie, Q. Shao, Z. Sun, Z. Guo, Large scaled synthesis of heterostructured electrospun TiO_2/SnO_2 nanofibers with an enhanced photocatalytic activity. J. Electrochem. Soc. **164**, H651–H656 (2017)
37. L. Zhang, M. Qin, W. Yu, Q. Zhang, H. Xie, Z. Sun, Q. Shao, X. Guo, L. Hao, Y. Zheng, Z. Guo, Heterostructured TiO_2/WO_3 nanocomposites for photocatalytic degradation of toluene under visible light. J. Electrochem. Soc. **164**, H1086–H1090 (2017)
38. Y. Zhang, L. Qian, W. Zhao, X. Li, X. Huang, X. Mai, Z. Wang, Q. Shao, X. Yan, Z. Guo, Highly efficient Fe-N-C nanoparticles modified porous graphene composites for oxygen reduction reaction. J. Electrochem. Soc. **165**, H510–H516 (2018)
39. B. Song, T. Wang, H. Sun, Q. Shao, J. Zhao, K. Song, L. Hao, L. Wang, Z. Guo, Two-step hydrothermally synthesized carbon nanodots/WO_3 photocatalysts with enhanced photocatalytic performance. Dalton Trans. **46**, 15769–15777 (2017)
40. X. Lou, C. Lin, Q. Luo, J. Zhao, B. Wang, J. Li, Q. Shao, X. Guo, N. Wang, Z. Guo, Crystal-structure modification enhanced $FeNb_{11}O_{29}$ anodes for lithium-ion batteries. ChemElectroChem **4**, 3171–3180 (2017)
41. C. Lin, H. Hu, C. Cheng, K. Sun, X. Guo, Q. Shao, J. Li, N. Wang, Z. Guo, Nano-$TiNb_2O_7$/carbon nanotubes composite anode for enhanced lithium-ion storage. Electrochim. Acta **260**, 65–72 (2018)
42. Q. Hou, J. Ren, H. Chen, P. Yang, Q. Shao, M. Zhao, X. Zhao, H. He, N. Wang, Q. Luo, Z. Guo, Synergistic hematite-fullerene electron extracting layers for improved efficiency and stability in perovskite solar cells. ChemElectroChem **5**, 726–731 (2018)
43. Y. Li, T. Jing, G. Xu, J. Tian, M. Dong, Q. Shao, B. Wang, Z. Wang, Y. Zheng, C. Yang, Z. Guo, 3-D magnetic graphene oxide-magnetite poly(vinyl alcohol) nanocomposite substrates for immobilizing enzyme. Polymer **149**, 13–22 (2018)
44. C. Wang, M. Zhao, J. Li, J. Yu, S. Sun, S. Ge, X. Guo, F. Xie, B. Jiang, E. Wujcik, Y. Huang, N. Wang, Z. Guo, Silver nanoparticles/graphene oxide decorated carbon fiber synergistic reinforcement in epoxy-based composites. Polymer **131**, 263–271 (2017)
45. J. Zhao, L. Wu, C. Zhan, Q. Shao, Z. Guo, L. Zhang, Overview of polymer nanocomposites: computer simulation understanding of physical properties. Polymer **133**, 272–287 (2017)
46. X. Cui, G. Zhu, Y. Pan, Q. Shao, C. Zhao, M. Dong, Y. Zhang, Z. Guo, Polydimethylsiloxane-titania nanocomposite coating: fabrication and corrosion resistance. Polymer **138**, 203–210 (2018)
47. C. Wang, B. Mo, Z. He, C.X. Zhao, L. Zhang, Q. Shao, X. Guo, E. Wujcik, Z. Guo, Hydroxide ions transportation in polynorbornene anion exchange membrane. Polymer **138**, 363–368 (2018)
48. Y. He, S. Yang, H. Liu et al., Reinforced carbon fiber laminates with oriented carbon nanotube epoxy nanocomposites: magnetic field assisted alignment and cryogenic temperature mechanical properties. J. Colloid Interface Sci. **517**, 40–51 (2018)
49. Z. Wu, S. Gao, L. Chen, D. Jiang, Q. Shao, B. Zhang, Z. Zhai, C. Wang, M. Zhao, Y. Ma, X. Zhang, L. Weng, M. Zhang, Z. Guo, Electrically insulated epoxy nanocomposites reinforced

with synergistic core-shell SiO_2@MWCNTs and montmorillonite bifillers. Macromol. Chem. Phys. **218**, 1700357 (2017)
50. Y. Zheng, Y. Zheng, S. Yang, Z. Guo, T. Zhang, H. Song, Q. Shao, Esterification synthesis of ethyl oleate catalyzed by Brønsted acid-surfactant-combined ionic liquid. Green Chem. Lett. Rev. **10**, 202 (2017)
51. Y. Zheng, Y. Zheng, Z. Wang, Y. Cao, Q. Shao, Z. Guo, Sodium dodecyl benzene sulfonate-catalyzed reaction for aromatic aldehydes with 1-phenyl-3-methyl-5-pyrazolone in aqueous media. Green Chem. Lett. Rev. **11**, 217–223 (2018)